BL1A

Formation of Active Mo Species Supported on SiO_2-Al_2O_3 for Dehydroaromatization:Mo L_{III}-edge XANES Study

H. Aritani,* M. Tamai,** K. Konishi,** S. Nishida,**
F. Nishimura,** and A. Nakahira**

**Faculty of Engineering, Saitama Institute of Technology, Okabe, Saitama 369-0293, Japan*
***Faculty of Engineering & Design, Kyoto Institute of Technology, Kyoto 606-8585, Japan*

MoO_3-modified H-MFI shows high activity for dehydroaromatization of methane, although strong deactivation cannot be avoided during the reaction. In this reaction, many workers have been revealed reduction of Mo species is brought about in contact with methane in the initial step. Deoxidated Mo ions react methane to form carbide species, Mo_2C, in the second stage. The carbide species is active for dehydroaromatization of methane to form benzene, however, deactivation is brought about by carbon deposition on the catalyst surface at the same time. It is likely the catalytic activity and its deactivation rate depend on the type of silica-alumina supports. Relation between silica-alumina support and active Mo species formed in the reaction is important to clarify the formation process of highly active Mo species and its red-ox behavior during the reaction. In fact, molybdena species supported on amorphous silica-alumina shows dehydroaromatization activity while it is very lower than that on H-MFI support. By comparing H-MFI with amorphous silica-alumina supports, reduction behavior of Mo ions before/after the reaction can be provided. Characterizaiton of those species by means of Mo L-edge XANES is appropriate for clarification of Mo ions with different valences. In this report, local structure of supported Mo ions on H-MFI and amorphous silica-alumina (SAH-1) and their redox changes after dehydroaromatization of methane or ethane at 973 K for 3 h is evaluated by Mo L_{III}-edge XANES.

Experimental

Mo L_{III}-edge XANES spectra were measured in BL1A of UVSOR-IMS in total-electron yield (TEY) mode, using the Ge(111) double-crystal monochromator ($2d$ = 0.6532 nm). The photon energy was calibrated by using Mo metal sample at Mo L_{III}-edge (2520 eV).

Results and Discussion

Fig. 1 shows the XANES spectra of authentic Mo samples. It is clear that both intensity and energy positions of two white-lines are different between Na_2MoO_4 (consist of $Mo^{6+}O_4$ tetrahedra, T_d) and MoO_3 (Mo^{6+}-O_6 octahedra, distorted O_h) because of local symmetry around Mo^{6+} ions. In cases of Mo_2C (Mo^{2+}) and Mo metal, edge energy values of those XANES are lower than Mo^{6+} samples, however, difference of edge energy is unclear between Mo_2C and Mo metal. To clarify the difference, second derivative XANES were introduced, as shown in Fig. 2. As for the 2nd derivative waves, minimum peaks are due to peak components of original XANES. The difference of energy value is significantly between Mo_2C (2524.2 eV as lowest energy) and Mo mettal (2523.5 eV). The assignment can be applied to the catalyst samples with reduced Mo ions. Fig. 3 shows the XANES spectra of MoO_3/SAH-1 and MoO_3/H-MFI catalysts before/after the reaction with CH_4 or C_2H_4 at 973 K. For MoO_3/SAH-1, it is concluded that reduced Mo species are formed after C_2H_4 reaction but not formad after CH_4 reaction. In case of MoO_3/H-MFI, which shows high catalytic activity for converting CH_4 to C_6H_6, several components due to Mo^{2+}- and Mo^{6+}- (peak at 2526.5 eV) species are overlapped after CH_4 reaction. This result suggests the formation of so-called "oxy-carbide species" as catalytically active species for dehydroaromatization of CH_4. After C_2H_4 reaction, Mo^{2+}-species is only formed and the component due to Mo^{6+}-species is scarcely seen. The reactivity for converting C_2H_4 to C_6H_6 is higher in MoO_3/SAH-1 than in MoO_3/H-MFI. In addition, crystallinity of MFI-phase in MoO_3/H-MFI became low only by the reaction with C_2H_4 by XRD analysis, suggesting catalytic deactivation during the reaction. Thus it is concluded that difference between H-MFI and SAH-1 supports gives the formation of Mo species with different reduction state after the reaction with CH_4. Partly reduced oxy-carbide species coexisting Mo^{2+} and Mo^{6+} ions are formed on H-MFI support after contact with CH_4, and this species can act as highly active species for CH_4 dehydroaromatization.

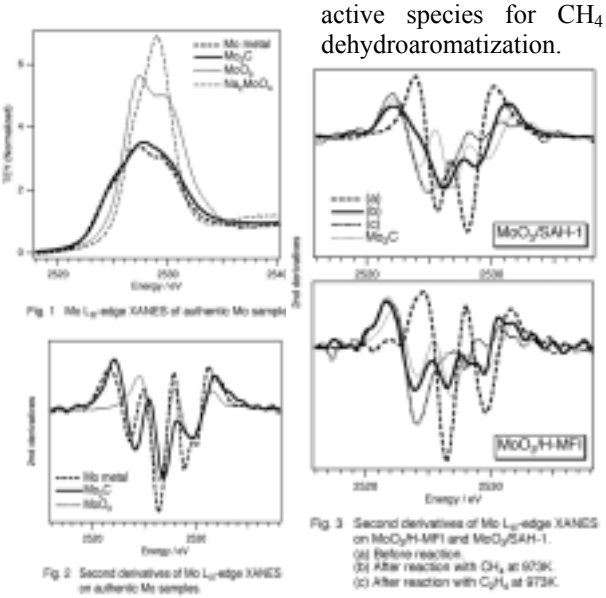

Fig. 1 Mo L_{III}-edge XANES of authentic Mo samples

Fig. 2 Second derivatives of Mo L_{III}-edge XANES on authentic Mo samples

Fig. 3 Second derivatives of Mo L_{III}-edge XANES on MoO_3/H-MFI and MoO_3/SAH-1.
(a) Before reaction
(b) After reaction with CH_4 at 973K
(c) After reaction with C_2H_4 at 973K

BL1A,8B1

Charging Mechanism of $Li_{1-x}Ni_{1/3}Mn_{1/3}Co_{1/3}O_2$ Cathode Materials for Lithium-ion Secondary Batteries from Transition Metal *L*-edge and Oxygen *K*-edge Spectroscopy

Y. Arachi, T. Asai, H. Kobayashi[†], S. Emura[††]

Faculty of Engineering, Kansai University, Osaka 564-8680, Japan

[†]National Institute of Advanced Industrial Science and Technology(AIST),Osaka 563-8577

[††]ISIR, Osaka University, Ibaraki, Osaka 567-0047

The alternatives to $LiCoO_2$ cathode material have been extensively searched due to small natural deposits of Co and its toxicity in the filed of Li-ion rechargeable batteries. Recently, $LiNi_{0.5}Mn_{0.5}O_2$ and $LiNi_{1/3}Mn_{1/3}Co_{1/3}O_2$ have been proposed as a new promising candidate.[1] Cell performance using Li exhibited good cycleability, and a reversible capacity of 150 mAh/g within the voltage range of 3.0 to 4.3 V, which corresponds to one-half of theoretical capacity (280mAh/g). We have employed the X-ray diffraction and XAFS measurement using synchrotron radiation source to investigate the structural change and the charging process of these materials.[2,3,4] In this study, the electronic structural change and the charging mechanism were investigated by XANES spectra of Co, Ni, Mn K- and L-edges, and O K-edge respectively.

Experiment

$LiNi_{1/3}Mn_{1/3}Co_{1/3}O_2$ was synthesized in air at 1273 K for 24 h using appropriate molar ratios of $LiOH{\cdot}H_2O$, $Mn(CH_3COO)_2{\cdot}6H_2O$, $Ni(CH_3COO)_2{\cdot}6H_2O$, and $Co(CH_3COO)_2{\cdot}6H_2O$ and de-lithiated samples were electrochemically prepared using coin-type cells with Li/1M $LiPF_6$ in EC:DEC(1:1)/samples. The Ni/Mn/Co valence states of samples were determined by the Ni/Mn/Co *K*-edge XANES spectra. X-ray absorption measurements at the Co, Ni, Mn L-edges and O K-edge by total electron yield were performed on BL1A and BL8B1.

Results and Discussions

$LiNi_{1/3}Mn_{1/3}Co_{1/3}O_2$ showed a single phase adopted the α-$NaFeO_2$ structure like as $LiCoO_2$. The results of the Ni, Mn and Co K-edge XANES spectra showed that $LiNi_{1/3}Mn_{1/3}Co_{1/3}O_2$ could be represented as $Li(Ni^{2+}_{1/3}Mn^{4+}_{1/3}Co^{3+}_{1/3})O_2$. On the other hand, Neutron diffraction measurements demonstrated that the lattice parameters of $LiNi_{1/3}Mn_{1/3}Co_{1/3}O_2$ are a = 2.860 Å and c = 14.22 Å and that the chemical composition can be expressed as $[Li_{0.97}Ni_{0.03}]_{3a}[Li_{0.03}Mn_{0.33}Ni_{0.30}Co_{0.33}]_{3b}O_2$, referring to the Wyckoff positions 3*a* and 3*b* with space group *R3m*. Figure 1 shows the XANES spectra of Ni L-edge for charged $Li_{1-x}Ni_{1/3}Mn_{1/3}Co_{1/3}O_2$. A continuous chemical peak shifts corresponding to L_{III}, L_{II} to higher energy was observed up to x = 0.7 for showing charge capacity of 194 mAh/g. The results of K-edge were observed in the same way. In addition, that of Co L-edge showed a slightly higher shift and that of Mn L- and K-edges showed no chemical shifts for all the samples. However, a systematic change was not clearly observed in O K-edge absorption. On the basis of these results, we are constructing the band structure and investigating the charging mechanism for this material.

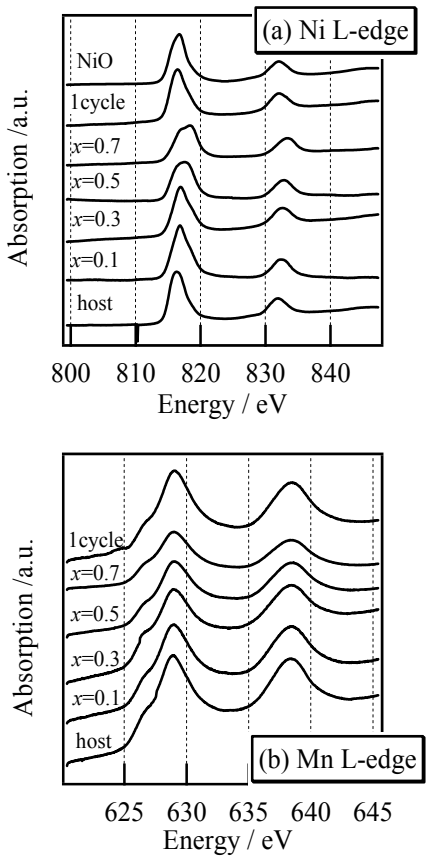

Fig.1 (a) Ni L- and (b) Mn L-edges XANES of $Li_{1-x}Ni_{1/3}Mn_{1/3}Co_{1/3}O_2$

1. T.Ohzuku and Y.Makimura,*Chem.Lett.*,(2001)744.
2. Y.Arachi, et al, *Chem.Lett.,* (2003)60.
3. H. Kobayashi et al., *J. Mater. Chem.*,14(2004) 40.
4. Y. Arachi et al., *Physica Scripta,* in press.

BL1A

Application of Synchrotron EXAFS on Studying Biomaterial

J. Ding[1,2], B. H. Sun[1], T. X. Fan[1], D. Zhang[1]
M. Kamada[3], K. Kuwahara[3], H. Ogawa[3], Q. X. Guo[4]
1. State Key Lab of MMCs, Shanghai Jiao Tong University, Shanghai 200030, P. R. China
2. Venture Business Laboratory, Saga University, Saga 840-8502, Japan
3. Synchrotron Light Application Center, Saga University, Saga 840-8502, Japan
4. Department of Electrical and Electronic Engineering, Saga Univ., Saga 840-8502, Japan

Porous materials are of scientific and technological interest because of their ability to interact with atoms, ions and molecules not only at their surfaces, but also throughout the bulk of the material [1]. These materials are extremely useful in catalysis and separation technologies [2]. Recently, novel porous morph-genetic ceramics synthesized from natural materials such as wood, fibers, surfaces of leafs, has recently attained particular interest [3, 4], because natural materials exhibit a hierarchically built anatomy optimized in the genetic evolution process, compared to artificial synthetic templates, and are abundant, cheap, renewable and environmentally conscious.

The porous morph-genetic ceramics is generally fabricated through sintering treatment at high temperature, after infiltrating various organic or inorganic solutions to the bio-template. Therefore, clarifying the mechanism of sintering process is indispensable for obtaining desired porous morph-genetic ceramics, because the sintering treatment plays a critical role for transforming the hierarchical cellular structure of bio-template into porous ceramics with specific functional properties. Unfortunately, it is impossible to reveal the dynamic transition during sintering process by using conventional analysis techniques such as scanning electron microscopy or X-ray diffraction. It is well known that extended X-ray absorption fine structure (EXAFS) is a powerful technique for determining the local structure with atomic selectivity in both crystalline and amorphous states. Therefore, we believe that it is possible to reveal the dynamic transition during sintering process by studying the local structure of atoms. However, to our best knowledge, no study of local structural properties of the porous morph-genetic ceramics has been reported up to now.

In this work, we investigate the local structural properties of the novel porous morph-genetic silicon carbide sintered at different temperatures by EXAFS for the first time. By measuring and analyzing Si K-edge EXAFS, it is found that the coordination number of nearest Si-Si shell dramatically changes when the structure is transformed from amorphous into crystalline, indicating the EXAFS technique is a useful tool to elucidate the synthesis mechanism for these novel porous morph-genetic ceramics.

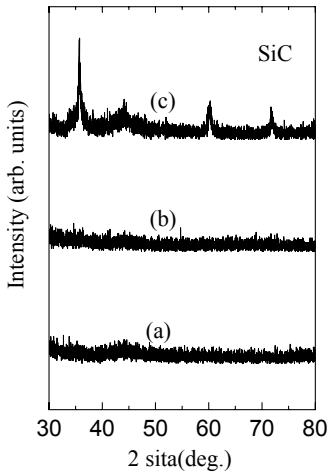

Fig. 1. XRD spectra of the samples sintered at temperatures of (a) 1273K, (b) 1473K, and (c) 1673K.

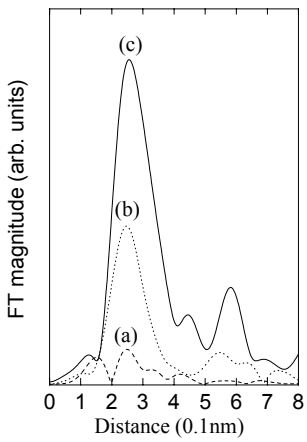

Fig. 2. Fourier transforms of Si K-edge EXAFS with weight κ^3, (a) 1273K, (b) 1473K, and (c) 1673K.

[1] M. E. Davis: Nature **417** (2002) 813.
[2]H. Yang, A. Kuperman, N. Coombs, S. Mamiche-Afara and G. A. Ozin: Nature **379** (1996) 703.
[3] P. Greil: J. Eur. Cera. Soc. **21** (2001) 105.
[4] A. Dong, Y. J. Wang, Y. Tang, N. Ren, Y. H. Zhang, Y. H. Yue and Z. Gao: Adv. Mater. **14** (2002) 926.

BL1A

First-Principles Study of Al K-edge NEXAFS Spectra of AlN and Al_2O_3

T. Yamamoto*, T. Suga*, S. Yoshioka, S. Kameyama and I. Tanaka
*Fukui Institute for Fundamental Chemistry, Kyoto University, Kyoto 606-8103, Japan
Department of Materials Science and Engineering, Kyoto University, Kyoto 606-8501, Japan

It has been well established that the X-ray absorption near-edge fine structure (NEXAFS) measurement is a powerful tool to analyze electronic structures of materials, because spectral fine structure of the NEXAFS spectrum is very sensitive to a change in chemical environment. Recently we have succeeded the chemical state analysis of the ultradilute Ga dopant at a level of atomic p.p.m in MgO matrix by combined use of the experimental NEXAFS analysis and the first-principles calculations [1]. For the chemical state analysis of lighter dopant elements by the NEXAFS within the soft X-ray region, we have performed preliminary NEXAFS measurement and the first-principles calculations for Al_2O_3 and AlN at Al K-edge. Our present calculations could quantitatively reproduce both a) spectral fine structure and b) transition energy of the experimental NEXAFS.

Experiments and calculations

High-resolution X-ray absorption spectra at the Al K-edge of Al_2O_3 and AlN were measured using the BL1A beamline at UVSOR. The NEXAFS spectra were collected by the total electron yield (TEY) method. The incident photon beam was monochromatized using a KTP ($2d_{011}$=10.954Å) double-crystal monochromator. Commercially available high purity powders with corundum and wurtzite types of structures for Al_2O_3 and AlN, respectively, were attached to the first photocathode of the electron multiplier using adhesive carbon tape. The crystal structures and contaminants of the sample employed here were checked by the X-ray diffraction (XRD) measurements, which revealed the presence of only small amounts of contaminants.

The first-principles density functional theory (DFT) calculations were carried out by using the full-potential linearized augmented plane wave package, WIEN2k [2]. The core-hole effect was fully introduced in our present calculations by using the 2x2x1 and 3x3x2 supercells for Al_2O_3 (120 atoms) and AlN (72 atoms), respectively. The theoretical NEXAFS spectra were calculated within the electronic-dipole-allowed transitions in the core-hole state. Product of the radial transition probability and corresponding projected partial densities of the states (*p*-PDOS) represents the theoretical NEXAFS spectrum.

Results

The observed NEXAFS spectra of Al_2O_3 and AlN at Al K-edge are shown in Fig. 1(a). Seven peaks, labeled as peaks A to G for Al_2O_3 and peaks J to P for AlN, were found within this energy regime in both Al_2O_3 and AlN. Theoretical NEXAFS spectra are shown in Fig. 1(b). As shown in this figure, the theoretical spectral features showed fairly good agreements with experimental ones. It is noted that experimental threshold energy shift, i.e., chemical shift, by 4.3 eV was also well reproduced by our present calculations, although absolute transition energies were slightly overestimated by 4.0 eV ($\Delta E/E = +0.25\%$).

In summary, we have carried out the NEXAFS measurements of Al_2O_3 and AlN at Al K-edge and the first-principles DFT calculations to interpret the spectral features and transition energy of experimental NEXAFS. Our present theoretical approach could give a quantitative reproduction of the experimental spectral fine structures and transition energies. This type of combined use of the experimental NEXAFS and the first-principles calculations must be a powerful tool for systematic and quantitative analysis of the chemical environment of the materials.

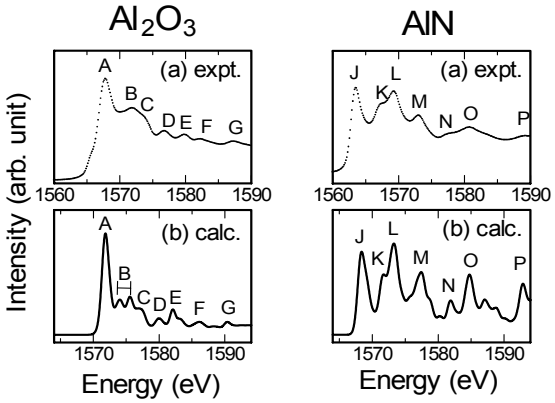

Fig. 1. Comparison of Al K-edge NEXAFS spectra of Al_2O_3 (left) and AlN (right) between (a) experiment and (b) calculation.

[1] I.Tanaka et al., Nature Materials 2 (2003) 541.
[2] http://www.wien2k.at

BL1A

Cl K XANES Analysis of the Electronic Structure around Metal Ion in Metallotetraphenylporphyrin

H. Yamashige, T. Kurisaki, H. Wakita*
Department of Chemistry, Faculty of Science, Fukuoka University, Nanakuma, Jonan-ku, Fukuoka 814-0180, Japan
**Advanced Materials Institute, Fukuoka University, Nanakuma, Jonan-ku, Fukuoka 814-0180, Japan*

The metallotetraphenylporphyrins (MTPPs) is of particular interest due to many possible applications, such as catalysts, electronic devices, gas sensors, and electroluminescent displays. MTPP have a large p-conjugated aromatic system. In order to elucidate chemical and physical properties of MTPP, it is necessary to determine their electronic structure [1].
In this work, we applied X-ray absorption near edge structure (XANES) spectroscopy to two type porphyrins, FeTPP-Cl and MnTPP-Cl. The results of the measurement indicate unoccupied and occupied electronic structure of MTPPs. The X-ray absorption spectra were measured at BL1A of the UVSOR in the Institute of Molecular Science, Okazaki [2]. The ring energy of the UVSOR storage ring was 750MeV and the stored current was 110-230 mA. Cl K-edge absorption spectra were recorded in the regions of 2533-3733eV by use of two Ge(111) crystals. The absorption was monitored by the total electron yield using a photomultiplier.
The Cl K-edge XANES spectra for the MTPPs are shown in Figs. 1 and 2. A remarkable change of the spectral patterns was observed for the FeTPP-Cl and MnTPP-Cl. Comparison of observed and calculated spectra revealed that metal 3d and 4p orbits contribute to peak A and B. But, MnTPP-Cl did not contain contribution from the Cl4p and Cl5p orbits.

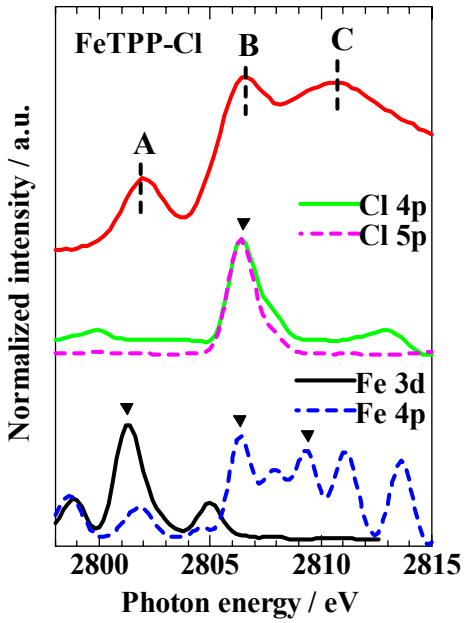

Fig. 1. Observed and calculated Cl K-edge XANES spectra of FeTPP-Cl.

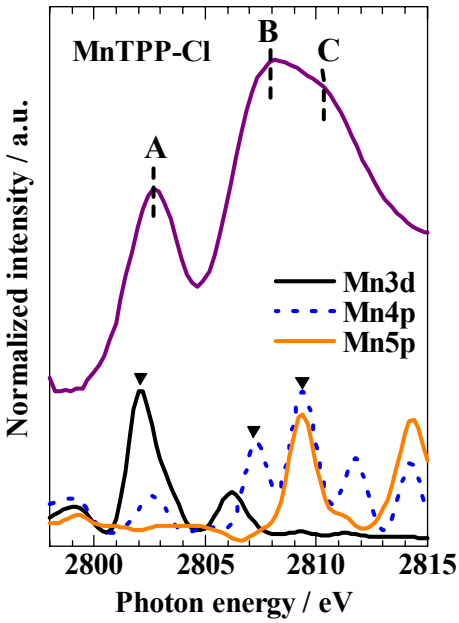

Fig. 2. Observed and calculated Cl K-edge XANES spectra of MnTPP-Cl.

[1] T. Okajima, Y. Yamamoto, Y. Ouchi and K. Seki, *Journal of Electron Spectroscopy and Related Phenomena*, 849 (2003)
[2] S. Murata, T. Matsukawa, S. Naoe, T. Horigome, O. Matsuodo, and M. Watatabe, Rev. Sci. Instrum., 63, 1309 (1992)

BL1A, 7A

The Measurement of γ and Soft X-ray Excited Optical Luminescence of a Silica Glass

T. Yoshida[1], T. Tanabe[1] and H. Yoshida[2]

[1]*Dept. of Nuclear Engineering, Graduate School of Nagoya University, Nagoya 464-8603*

[2]*Dept. of Applied Chemistry, Graduate School of Nagoya University, Nagoya 464-8603*

In the present work, we have made in-situ luminescence measurements of silica glasses induced by γ-ray and soft X-ray, on silica. The main objects of this report are to clarify of the dynamic damaging process in silica which should be induced by the electron excitation, as well as the difference of the radiation effects between γ-ray and soft X-ray irradiations.

Experimental

The measurement of luminescence of the fused silica glass induced by soft X-ray irradiation (1.8-1.9 keV) was carried out on the beam line 7A at UVSOR, Institute for Molecular Science with a stored current of 100-200 mA. The size of soft X-ray beam was ca. 2 x 10 mm, and the flux was ca. 1 x 10^9 photons / mm^2/ sec / 100 mA. The luminescence was focused by a lens in the UHV chamber to the monochromator and detected by a multi-channel analyser.

Results and Discussion

Fig. 1 shows the soft X-ray induced luminescence of the fused silica glass. The 3.1 eV band attributed to $B_{2\beta}$ center was observed. One notes the significant deviation of the 3.1 eV band intensity profile for the different excitation energies of the incident soft X-ray. Irrespective of the incident energy of soft X-ray, fundamentally the same evolutions were observed. The intensity of the 3.1 eV band slightly increased in the early stage of the irradiation and then decayed gradually with irradiation time, similarly to the change of the 3.1 eV emission band in the γ-ray induced luminescence.

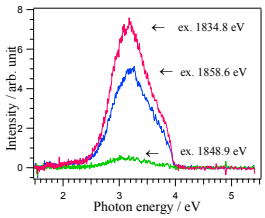

Fig.1 Optical luminescence spectra of a fused silica glass under the irradiation of soft X-ray with the energy of 1834.8 eV, 1848.9 eV and 1858.6 eV

Such changes of luminescence induced by the soft X-ray irradiations, must be discussed based on absorbed dose (Gy = J/kg) and absorbed dose rate. The absorbed dose rate (Gy/sec) for the γ-ray irradiation was evaluated as ca. 1.6 Gy/sec. On the other hand, in the case of soft X-ray irradiation, the absorbed dose rate changes drastically around the Si K-edge, because the penetration depth of the soft X-ray above the K-edge is much shorter than that below the K-edge in accordance with the change of the absorption coefficient (μ) of a silica glass. On the basis of the value of μ , we roughly estimated the penetration depths of soft X-ray below and above the edge as 5 x 10^{-3} and 2 x 10^{-4} cm, respectively. Accordingly the absorbed dose rates were estimated as ca. 2.6 and 12.9 Gy/sec, for 1834.8 eV and 1848.9 eV(1858.6 eV), respectively. Then we can obtain normalized luminescence yield from the intensities of the 3.1 eV emission band during both γ- and soft X-ray irradiations divided by the following two factors, i.e., (1) the volumes of the silica glass where γ- and soft X- rays were absorbed and (2) the detecting efficiencies of the spectrometers.

The normalized luminescence yields of the 3.1 eV band thus obtained are plotted against the absorbed dose in Fig. 2. One can note that all normalized yields show similar dependence on the absorbed dose, in spite of the large difference between γ- and soft X-rays energies. The normalized intensities rapidly increased and reached the maximum at around 3.5 kGy, followed by a gradual decrease. It is noteworthy that all the normalized yields are within a factor of 10, which is far less than the energy difference of γ-ray and X-ray (three order's of magnitude). This means that the luminescence is controlled by the absorbed dose, in other words, the luminescence is induced by the electron excitation from secondary electrons and photons with low energies, but not by the direct excitation of primary (Compton) or high energy electrons and photons.

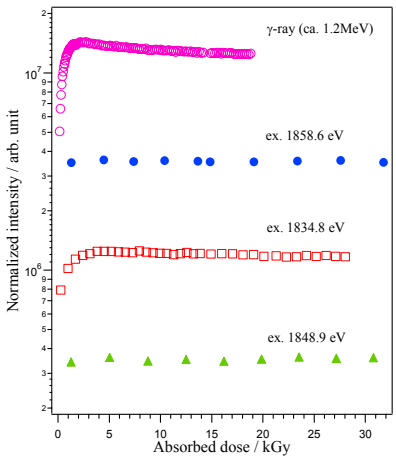

Fig.2 The variation of the normalized intensities of 3.1 eV band with the absorbed dose under the irradiation of γ-ray and soft X-ray with the energy of 1834.8 eV, 1848.9 eV and 1858.6 eV.

BL2B1

Photoemission Study for Initial Oxidation and Nitridation of ZrB_2

K. Takahashi, S. Tokudomi*, Y. Nagata*, K. Fukui**, M. Kamada
Synchrotron Light Application Center, Saga University, Saga 840-8502 Japan
**Faculty of Science and Engineering, Saga University, Saga 840-8502 Japan*
***Research Center for Development of Far-Infrared Region, Fukui University, Fukui 910-8507 Japan*

Transition metal diborides are attractive materials due to its hardness, high-melting point and chemical stability. Among then, zirconium diboride (ZrB_2) has the hexagonal symmetry of the AlB_2-type structure with an in-plane lattice constant of 0.3168 nm which is very close to that of GaN. Recently, epitaxial growth of GaN film on ZrB_2 substrate has succeeded using the metal-organic vapor phase epitaxial method. In order to obtain epitaxial GaN film with good crystallinity, it is indispensable to elucidate the initial oxidation and nitridation processes. In addition, after the unexpected discovery of high temperature superconductivity in MgB_2, diborides have attracted renewed attentions. In this work, we have performed the photoemission study for clean $ZrB_2(0001)$ surface obtained by in-situ annealing treatment and its initial oxidation and nitridation processes.

Experimental

Experiments have been performed at beamline BL2B1. The $ZrB_2(0001)$ single crystalline sample was grown by floating-zone method. The $ZrB_2(0001)$ sample was fixed on the molybdenum tile using a small molybdenum clip. The clean surface was obtained by the repetition of flash annealing around 1850ºC. The base pressure of the measurement chamber was about 2×10^{-8} Pa. The pressure during the flash annealing was kept better than 5×10^{-7} Pa. The O_2 and N_2 were exposed up to 100 Langmuir (1L = 1×10^{-6} Torr×s) at 650ºC. The photoemission spectra were obtained using the double-pass cylindrical mirror analyzer. The overall energy resolution was about 1.3eV.

Results and Discussions

Figure 1 shows the photoemission spectra for B 1s and Zr 3d core-levels. The peaks at 179.0, 181.3 and 187.7 eV in binding energy correspond to Zr $3d_{5/2}$, Zr $3d_{3/2}$ and B 1s core-levels, respectively. Since the spectrum for the clean surface shows no structure originated from the oxidized component, we conclude that contamination free surface can be obtained using our cleaning procedure. The sample showed sharp hexagonal low-energy electron diffraction pattern after the cleaning procedure. We have also performed separated UPS measurements for clean $ZrB_2(0001)$ surface. The work function of the clean $ZrB_2(0001)$ surface is determined from the width of the photoemission spectra to be 5.1±0.1 eV, which is much larger than that of polycrystalline boron (4.5 eV). On a $LaB_6(100)$ surface, the charge transfer occurs form La to B atoms and the dipole moment is directed from the surface into the bulk since the outermost layer of the $LaB_6(001)$ surface consists of La atoms. As a result, the work function of $LaB_6(001)$ is as small as 2.5 eV. From our result, it is considered that the clean surface of $ZrB_2(0001)$ is terminated by graphitic-boron layer and the charge transfer form the second Zr layer to the first B layer exist. Because of the B atom at the $ZrB_2(0001)$ surface, the dipole moment is directed outward, and the work function is increased. As shown in Fig.1, the new components appear at 182.0 and 184.3 eV in binding energy after a 11 L O_2 exposure at 650ºC. The chemical displacement of +3.0 eV is smaller than that between Zr and ZrO_2. The literature value of chemical shift is 4.2 eV for Zr $3d_{5/2}$ between Zr and ZrO_2. On the other hand, the new components appear at lower binding energy after a N_2 exposure at 650ºC. It is found that the chemical displacement of Zr $3d_{5/2}$ core-level is -0.7 eV. We have also performed the X-ray absorption measurement in the N 1s-2p threshold region for 10 L N_2 exposed surface. It is found that the X-ray absorption spectra show the dependence on the indent photon direction. In order to clarify the bonding orientation of the chemisorbed N atoms on $ZrB_2(0001)$ surface, more detailed measurements is needed.

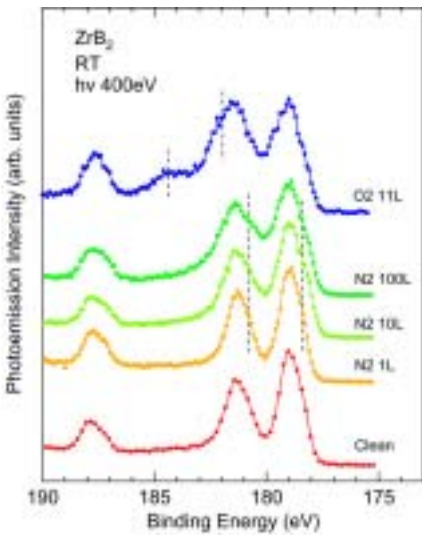

Fig. 1. Photoemission spectra for B 1s and Zr 3d core-levels.

BL4B

Electronic Structure of DNA Studied by Resonant Photoemission Spectroscopy

H. S. Kato, M. Furukawa, M. Kawai, M. Taniguchi*, T. Kawai*, T. Hatsui**, N. Kosugi**

RIKEN (The Institute of Physical and Chemical Research), Wako 351-0198 Japan
**Institute of Scientific and Industrial Research, Osaka University, Ibaraki 567-0047 Japan*
***UVSOR Facility, Institute for Molecular Science, Okazaki 444-8585 Japan*

The characterization of electronic states near Fermi level of DNA duplexes has been desired to clarify the mechanisms of long-range charge migration in DNA, from the viewpoint of not only biochemistry but also molecular device materialization. With the recent progress in nanotechnology, the electric conductivity of DNA has directly been measured in molecular scale. However, these characterizations of the electric property are still indefinite, and there is no significant observation on the electronic states near Fermi level of DNA for understanding of the charge migration mechanism. In this study, therefore, we carried out resonant photoemission spectroscopy (RPES) experiments near Fermi level with resonance from N 1s to unoccupied states for both poly(dG)·poly(dC) (GC) and poly(dA)·poly(dT) (AT) DNA duplexes.

Experimental

Experiments were performed at the beamline BL4B of the UVSOR facility, in which the end-station (ultrahigh vacuum systems) is equipped with an electron energy analyzer and a retarding-field electron detector for XAS. We prepared thick GC- and AT-DNA films on SiO_2/*p*-Si(111) substrates in the atmosphere. The film thickness prepared was estimated to be 100 - 200 nm. These samples were introduced into the ultrahigh vacuum via a sample entry system from the atmosphere, without baking procedures.

Results and Discussion

An N K-edge X-ray absorption (XA) spectrum of GC DNA is shown in the inset of Fig. 1. In the XA spectrum, two 1s - π* resonant peaks at 399.7 eV and 401.9 eV and a broad 1s - σ* resonant peak at 407 eV were observed. The off- / on-RPE spectra near the Fermi level of GC DNA are shown in Fig. 1 as a function of kinetic energy. The RPE spectra were measured at each resonant absorption peak marked on the XA spectrum shown in the inset. On the comparison to the off-RPE spectrum, the on-RPE spectra are obviously involving additional components which is attributed to the N-KLL Auger electrons.

The Auger signals could be extracted from the on-RPE spectra by subtracting the off-RPE spectra in binding energy plots, as the dotted lines in Fig. 1. The differential spectra commonly show a broad bump. Normally, the Auger electrons keep an identical distribution in kinetic energy, independently of excitation photon energies. The obtained Auger signals were, however, strongly affected by excitation energy; the lower photon energy light provides a higher kinetic energy distribution. This indicates that the excited electrons locate in the unoccupied states for, at least, a time scale of Auger transition and affect its final state of the transition.

In addition, an appended component was observed at the first π* resonance, as marked by a dagger in Fig. 1. We attribute the additional component to those of participant Auger transition. This finding again indicates that the excited electrons locate in the π* states for, at least, the time scale of Auger transition.

In the case of the molecules chemisorbed on metals, their RPE spectra do not show the drastic peak shift of Auger electrons in kinetic energy and also the participant Auger electrons. These are explained as that the molecular orbitals rehybridized with metal electronic states are delocalized, and the excited electrons in the chemisorbed molecules diffuse into the metal, immediately. In contrast, all features of the observed RPE spectra of DNA, as mentioned above, clearly show that the excited electron is localized at the excited orbitals. In other words, the unoccupied states of the bases in DNA duplexes are not delocalized. Hence, we conclude that the charge hopping model is suitable for electric conduction in DNA duplexes rather than the charge transfer model via delocalized states, when electrons pass through the π* states of the DNA bases.

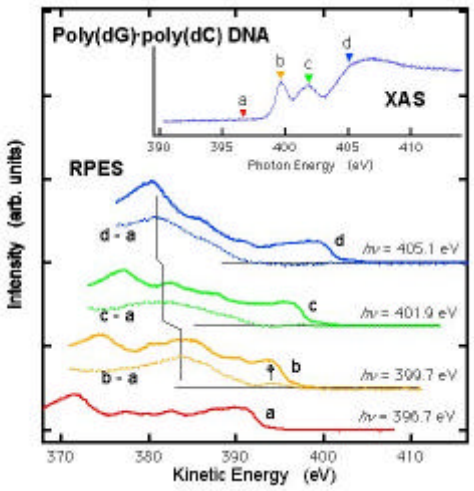

Fig. 1. Off- / on-RPE spectra of GC DNA. The inset shows an N K-edge X-ray absorption spectrum.

BL4B

Excited States of Ar 2p in Ar Solid

H. Setoyama, T. Hatsui and N. Kosugi

Institute for Molecular Science, Okazaki 444-8585 Japan

Rydberg states in condensed phase are of interest since they are sensitive to external perturbation due to their large orbital radii. Several studies have been carried out on surrounding effects in the Ar 2p excited states using rare gas matrixes. Changes of the spectral features between another condensed phases are explained by the competition of two effects, namely, (i) the polarization stabilization of the ionization threshold, and (ii) the exchange repulsion of the Rydberg electron due to the valence electrons of the neighboring atoms/molecules. [1] In the present study, temperature dependence of the peak position of the bulk Ar $2p_{3/2}$-4s band has been measured to reveal the latter effect. The exchange repulsion is mainly influenced by the inter-atomic distance between the neighboring atoms. Different temperatures of Ar solid make different inter-atomic distances of neighboring Ar. The different inter-atomic distance between the neighboring Ar should reveal the effect.

The Ar solid was prepared by dosing Ar gas approx. 30 L to the gold coated copper plate of a cryostat at ~8K. The temperature of the Ar solid was monitored using a silicon diode thermostat and was adjusted to 8K or 16K by using a ceramic heater. Photoabsorption spectra were measured by a partial electron yield (Auger yield) method using an MCP detector with a retarding mesh (-180V). All spectra were taken at grazing incidence angle of 15 degree. The photoabsorption spectra were taken for several times since there was an energy drifting (~7 meV per hour) caused by the instability of the beamline monochromator.

Fig. 1 shows the observed energy position of the Ar $2p_{3/2}$ –4s for bulk Ar atom measured at different temperatures, 8K and 16K. The typical spectra for 8K and 16K are also shown as inset. Photon energy was calibrated by using the bulk Ar $2p_{3/2}$ –4s band (245.06eV) for 8K Ar solid. [1] As shown in the inset, the main band is observed with a shoulder structure at the lower photon energy side. The main band is assigned to the transition from Ar $2p_{3/2}$ to 4s band of bulk Ar atom and the shoulder structure is assigned to that of surface Ar atoms. [1] Comparing with the main bands for 8K and 16K spectra, it is clearly seen that the spectral features are very similar but the bulk band shows different excitation energy. To obtain the excitation energies of the $2p_{3/2}$ –4s band of the bulk Ar atom for 16K, the photoabsorption spectra were taken for several times and the bands are fitted with two Voigt functions. In Fig. 1, the vertical axis indicates the uncalibrated energy positions of the Ar $2p_{3/2}$ –4s band. The horizontal axis indicates the measuring time. Error bars indicate 2σ of the peak fittings. The blue and red lines indicate the linear fittings for the energy driftings for 8K and 16K, respectively. The difference between the sections for both lines gives the excitation energy difference of 5 ±1.5 meV.

The temperature increase causes an expansion of the lattice constant of the Ar solid. The Ar solid has a face-centered cubic structure with the lattice constants of 5.2890 Å and 5.2941 Å for 8K and 16K, respectively. [2] Neighboring Ar atoms with shorter inter-atomic distance are expected to have stronger perturbation (exchange repulsion) because the excited electron in 4s-Rydberg states is pushed to higher energy side by closer potential of the surrounding Ar atoms. This can be explained as stronger exchange repulsion by the surrounding atoms arisen from shorter inter-atomic distance of 8K than 16K. The bulk Ar $2p_{3/2}$-4s band at 8 K shows blue shift of 5 ±1.5 meV from that at 16 K because of the increase of the exchange repulsion caused by the reducing the inter-atomic distance.

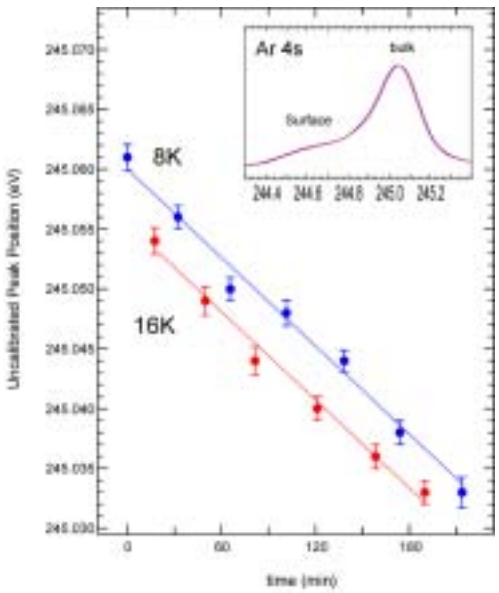

Fig. 1. The peak position of Ar 4s (bulk)

[1] T. Hatsui, M. Nagasono, N. Kosugi, *J. Electron Spectrosc. Relat. Phenom.,* in press.
[2] *Nonmetallic Solids*, Thermalphysical Proberties of matter, vol.13 Thermal expansion, Y.S.Touloukian, *et al.,* (IFI/Plenum, New York, 1997)

High-resolution Angle-resolved Photoemission Spectroscopy on CeSb

T. Ito, S. Kimura, H. Kitazawa*
UVSOR Facility, Institute for Molecular Science, Okazaki 444-8585 Japan
**Nano-Material Labolatory, National Institute for Materials Science (NIMS), Tsukuba 305-0047, Japan*

The anomalously complicated magnetic phase transition on CeSb has been intensively studied by both experiment and calculation. The origin has long been believed to be understood under the framework of Ce 4*f*-Sb 5*p* mixing model (*pf* mixing model) [1,2]. On the other hand, the recent optical and magneto-optical experiments suggest the importance of the Ce 5*d*-Sb 5*p* mixing effect from the comparison with the band structure calculation based on the *pf*+*pd* mixing model [3,4]. Thus, we have performed high-resolution angle-resolved photoemission spectroscopy (ARPES) on CeSb at the para- and type-IA antiferro magnetic (AF) phase to elucidate the appropriate starting point of the complicated magnetic phase transition.

ARPES measurements were carried out using a MBS Toyama A-1 electron analyzer with a GAMMADATA discharge lamp and a toroidal grating monochromator. Ce 4*d*-4*f* resonant ARPES measurements have been performed at UVSOR-II BL5U with using the hν=115 eV and 122 eV photons (ΔE=100 meV, Δθ=±0.1°), while high-resolution ARPES measurements with using He Iα photons (ΔE=15 meV, Δθ=±0.1°). The single crystals were cleaved on the (001) plane *in situ* under vacuum of 2 x 10^{-8} Pa to obtain a clean mirrorlike surface. The Fermi level (E_F) of the sample was referred to a gold film evaporated onto the sample substrate.

Figure 1 (a) and (b) shows the valence band structure of paramagnetic CeSb obtained by plotting the intensity of Ce 4*d*-4*f* off (hν=115 eV)- and on (hν=122 eV)-resonant ARPES spectra as a function of the wave vector and the binding energy. Bright areas correspond to "bands". From the comparison of the experimental band structure in Fig.1, highly-dispersive features at E_F-2 eV enhanced on the off-resonant ARPES are dominated by the valence Sb 5*p* and Ce 5*d* electrons, while a non-dispersive feature at 3 eV by the localized Ce 4*f* states. Furthermore, the residual spectral weight near E_F of on-resonant ARPES spectra may suggest the existence of hybridization between Ce 4*f* states and valence *pd* electrons, as clearly seen in Fig. 1 (c).

To elucidate the change of band structure through magnetic phase transition, we have performed temperature-dependent high-resolution ARPES on CeSb with using He Iα photons. Figs. 2 (a) and (b) show the "band structure" near E_F of CeSb around the Γ(*X*) point along the Γ*X*-*XWX* emission plane measured at the para- (*T*=30 K) and AF- (*T*= 5K) magnetic phase, respectively. Red and white areas correspond to "bands". From the para- to AF magnetic phase, we have observed two types of changes in the band structure near E_F. (1) The energy positions of the Sb 5*p* (A_1(') and A_2(')), and the Ce 5*d* bands (A_3(')) around the Γ(*X*) point approach each other (see Fig. 2(c)). (2) The additional band *B* with its top around 200 meV appears at AF-magnetic phase. While the former seems to be consistent with the *pf* mixing model, where the Sb 5*p* bands at the Γ point expect to be pushed up to E_F following the simultaneous downward shift of the Ce 5*d* bands [2], the latter is not explained by the model, since the band *B* is suggestive of the band energy-splitting, which has not been expected by the *pf* mixing model. On the other hand, we have found a qualitative agreement between the experiment and the recent calculation based on *pf*+*pd* mixing model [4], where the band energy-splitting originating in the *pf*+*pd* mixing effect along the Γ*X* axis has been expected. This result suggests the importance of the *pd* mixing effect to interpret the exact mechanism of the magnetic phase transition in CeSb other than the *pf* mixing effect.

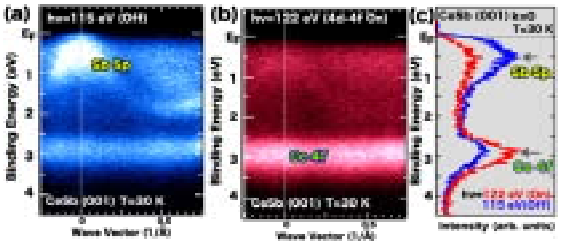

Fig. 1 (a, b) Comparison of the valence band structure of paramagnetic CeSb obtained by ARPES spectra with hν=115 eV (a) and 122 eV (b) photons.
(c) Comparison of normal emission ARPES spectra with hν=115 eV (blue line) and 122 eV (red

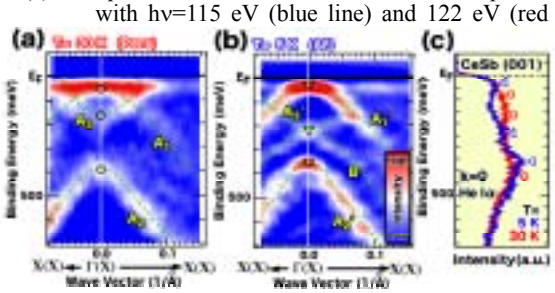

Fig. 2 (a, b) Experimental band structure of para- (a) and AF- magnetic (b) CeSb derived by ARPES. Dashed lines are guide for eyes.
(c) Comparison of normal emission ARPES spectra between AF- (blue line) and para-magnetic (red line) CeSb.

[2] H. Kumigashira *et al.*, Phys. Rev. B **56** (1997) 13654.
[3] S. Kimura *et al.*, J. Phys. Soc. Jpn. **71** (2002) 2200.
[4] S. Ishiyama and O. Sakai, J. Phys. Soc. Jpn. **72** (2003) 2071.

BL5U

Pseudo-gap in $Zr_{55}Al_{10}Cu_{30}Ni_5$ Bulk Metallic Glass

K. Soda, K. Shimba, M. Kato, S. Yagi, T. Takeuchi,* U. Mizutani
T. Zhang,**M. Hasegawa,** A. Inoue,** T. Ito,*** S. Kimura***
Graduate School of Engineering, Nagoya University, Furocho, Chikusa-ku, Nagoya 464-8603
**Research Center for Advanced Waste and Emission Management, Nagoya University, Furocho, Chikusa-ku, Nagoya 464-8603*
***Institute for Materials Research, Tohoku University, Katahira, Aoba-ku, Sendai 980-8577*
****UVSOR, Institute for Molecular Science, Myodaijicho, Okazaki 444-8585*

Bulk metallic glasses have received much attention as new materials which possess useful engineering properties such as high mechanical strength, good ductility, and high corrosion resistance. In order to understand the origins of the large glass formation ability and unique properties of the bulk metallic glass from the microscopic point of view, we have studied the electronic structure of a $Zr_{55}Al_{10}Cu_{30}Ni_5$ bulk metallic glass [1] by photoelectron spectroscopy.

Experimental

Photoelectron spectra were recorded under an ultrahigh vacuum of 2×10^{-8} Pa at low temperatures with a high-resolution energy analyzer at BL5U. Total energy resolution and the origin of the binding energy E_B, *i.e.* the Fermi level E_F, were determined by the Fermi edge of an evaporated Au film.

Specimens were cut from an ingot of $Zr_{55}Al_{10}Cu_{30}Ni_5$ into a size of 3x3x2 mm^3 and attached on a cupper plate by conductive glue. Clean surfaces for the photoelectron measurement were prepared by *in situ* scraping the specimen with a diamond file.

Results and Discussion

Figure 1 shows typical valence-band photoelectron spectra of $Zr_{55}Al_{10}Cu_{30}Ni_5$ recorded at 20 K with various excitation photon energies $h\nu$. They are normalized by the intensity integrated up to the binding energy E_B = 10 eV (exceptionally 7 eV for $h\nu$ ~22.3 eV). Three features at E_B ~0.6 eV, ~2.0 eV and ~3.7 eV in the valence band region are ascribed to the Zr 4*d*, Ni 3*d* and Cu 3*d* states, respectively, because of their $h\nu$ dependence [2]. An Auger line is also found at E_B ~ 8 eV for $h\nu$ = 66.8 eV.

Remarkable feature of the observed spectra is the highly symmetric shape of the transition metal *d* bands with the high binding energy and the narrow width in comparison with those of the crystalline transition metals. The Cu and Ni 3*d* band widths decrease from ~2 eV for crystalline Cu and Ni metals to ~1 eV for the glass. This is mainly due to the reduction in the neighboring atoms to hybridize with those transition metals in the glass. The symmetric shape may also arise from the lack of the crystalline periodicity.

In Fig.2, high-resolution spectra recorded with a He I light source ($h\nu$ = 21.2 eV) are presented for the valence-bands near E_F of the metallic glass and reference Au. Compared with Au, the intensity is reduced below E_B ~ 0.12 eV for the metallic glass. This suggests that a pseudo-gap is formed in this metallic glass, which may stabilize the glass phase and contribute to its large glass formation ability.

At present, however, it is not clear whether these aspects are intrinsic for the glass phase of this alloy or not. Further study is intended on the crystalline counterpart and the glass with different compositions.

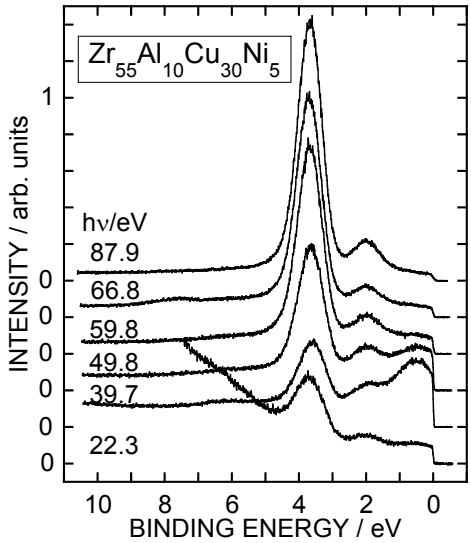

Fig.1 Valence-band spectra of $Zr_{55}Al_{10}Cu_{30}Ni_5$. The excitation photon energy $h\nu$ is indicated.

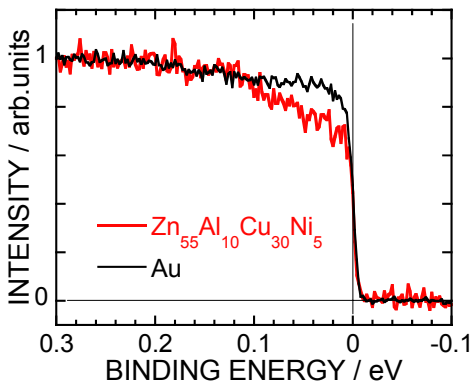

Fig.2 Valence-band spectra near the Fermi level of $Zr_{55}Al_{10}Cu_{30}Ni_5$and Au.

[1] A. Inoue and T. Zhang, Mat. Trans. JIM **37** (1996) 185.
[2] J. J. Yeh and I. Lindau, Atom. Data Nucl. Data Tables **32** (1985) 1.

BL5U

Evaluation of Thermoelectric Power in the Al-Mn-Re-Si 1/1-1/1-1/1 Approximant Using High-resolution Photoemission Spectroscopy

T. Takeuchi[1], T. Kondo[2], H.Takahashi[2], H. Sakagami[2], T. Otagiri[2], U. Mizutani[2], T. Itoh[3] and S. Kimura[3]

[1] *Research Center for Advanced Waste and Emission Management, Nagoya University, Nagoya 464-8603*

[2] *Department of Crystalline Materials Science, Nagoya University, Nagoya 464-8603*

[3] *UVSOR, Institute for Molecular Science, Okazaki 444-8585 Japan*

It has been widely believed that metallic compounds are inappropriate for their use as thermoelectric devices because their thermoelectric power, in general, possesses extremely small magnitude as low as a few μV/K. Recently, however, some metallic compounds such as quasicrystals and cobalt oxides were reported to show a large magnitude in the thermoelectric power. These experimental observations strongly motivated us to investigate the mechanism leading to the large thermoelectric power coupled with metallic electrical conduction.

Thermoelectric power of the metallic electrical conduction can be well explained by

$$S(T)=\frac{1}{eT}\frac{\int(\varepsilon-\mu)\sigma(\varepsilon)\frac{\partial f(\varepsilon)}{\partial\varepsilon}d\varepsilon}{\int\sigma(\varepsilon)\frac{\partial f(\varepsilon)}{\partial\varepsilon}d\varepsilon} \qquad (1)$$

where $\sigma(\varepsilon)$, μ, and $f(\varepsilon)$ indicate electrical conductivity, chemical potential, and Fermi-Dirac distribution function, respectively. Electrical conductivity in a isotropic system is determined by the following equation with in the context of the Boltzmann transport theory.

$$\sigma(\varepsilon)=\frac{e^2}{12\pi^3\hbar}S(\varepsilon)v(\varepsilon)\tau(\varepsilon)=\frac{e^2}{3\pi^3}N(\varepsilon)v^2(\varepsilon)\tau(\varepsilon) \qquad (2)$$

Here $N(\varepsilon)$, $v(\varepsilon)$, and $\tau(\varepsilon)$ represent electronic density of states, group velocity, and relaxation time, respectively. If $v(\varepsilon)$ and $\tau(\varepsilon)$ can be regarded as energy-independent in a narrow energy range where $\partial f(\varepsilon)/\partial\varepsilon$ has nonzero value while it turns out to possess negligibly small value at the outside of the energy range, $\sigma(\varepsilon)$ in eq.(1) can be simply replaced by N(e). In such a case, thermoelectric power can be evaluated using information about $N(\varepsilon)$. In this study, we employed high energy-resolution photoemission spectroscopy to investigate $N(\varepsilon)$ of the $Al_{74.6}Mn_{8.7}Re_{8.7}Si_8$ 1/1-1/1-1/1 approximant of the icosahedral quasicrystal. Thermoelectric power in the approximant was evaluated by the measured photoemission spectrum. The energy resolution of the present measurements was better than 20 meV.

Photoemission spectra, in general, are believed to have information only about the valence band below the Fermi level (E_F). However, those measured at high temperature contain information about the conduction band up to a few above E_F. If the measured spectrum is divided by $f(\varepsilon)$, the resulting spectrum ($N'(\varepsilon)$) gives us information about electronic density of states across E_F.

We calculate the thermoelectric power by using eq.(1) and the deduced $N'(\varepsilon)$. Although its magnitude stays less than half of the observed value, the calculated $S(T)$ shows almost the same temperature dependence as that of the measured one. If we take an energy independent contribution of the surface or grain boundaries into accont, the magnitude of S(T) is increased and the thermoelectric power can be perfectly determined from experi-mentally determined density of states. We have already applied this method for the layered cobalt oxides and the layered cuprates of the metallic electrical conduction and succeed in quantitatively evaluating their thermoelectric power.

As a result of these analyses on the thermoelectric power in terms of the electronic structure near E_F, we concluded that the large thermoelectric power with metallic electrical conduction is brought about by the characteristic electronic structure near E_F and is predictable if the electronic structure is precisely determined.

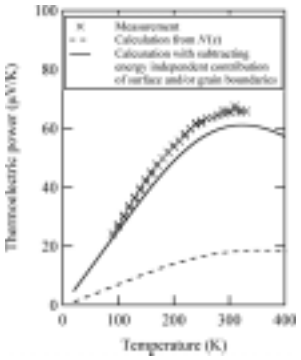

Figure 1 Measured and calculated $S(T)$. The calculated value with subtracting energy independent contribution of surface and /or grain boundaries form $N'(\varepsilon)$ shows extremely good consistency with the measured one.

BL5U

Dynamic Final-State Effect on the Core-Level Photoemission of Surface-Passivated Au Nanoparticles on the Graphite Substrates

A. Tanaka, Y. Takeda, M. Imamura, S. Sato

Dept. of Physics, Graduate School of Science, Tohoku University, Sendai 980-8578, Japan

Recently, the surface-passivated nanoparticles have been chemically synthesized in the solution including surfactants. These surface-passivated nanoparticles exhibit closed-packed nanoparticle self-assemblies on the single-crystalline substrates, and therefore it is considered that they could be important constituents of future nanostructured devices. In order to elucidate their detailed intriguing properties and to develop the future devices, it is indispensable to understand the interactions with the substrates supporting the nanoparticles as well as their electronic structures. In this work, we have carried out a photoemission study of dodecanethiolate- (DT-) passivated Au nanoparticles.

The synthesis procedure of DT-passivated Au nanoparticles has been described elsewhere [1-3]. Photoemission measurements were carried out at BL-5A of UVSOR Facility. For the photoemission measurements, the synthesized DT-passivated Au nanoparticles were supported on HOPG substrates by evaporating the solvent (toluene) from the dispersion of DT-passivated Au nanoparticles on the single-crystalline HOPG cleaved surface in a nitrogen-filled glove bag directly connected to the ultrahigh-vacuum chamber. Photoemission measurements were performed with the incident photon energy of 180 eV at room temperature.

The Au 4*f* core-level spectra of DT-passivated Au nanoparticles consist of the two components, and the components with lower binding energy and higher binding energy originate from the inner Au atoms of Au nanoparticles (bulk component) and the surface Au atoms of Au nanoparticles bonded to surface-passivants of DT molecules (surface component), respectively [2]. An important point to note here is that the bulk components shift to higher binding energy side with decreasing the nanoparticle diameter (not given here). In our previous work [1], we have reported that the photoemission spectra in the vicinity of Fermi-level of DT-passivated Ag nanoparticles on the HOPG substrates are well characterized by the dynamic final-state effect due to the photohole with a finite lifetime left behind in the nanoparticles in the photoemission final state. This finite lifetime is determined by the coupling strength between the nanoparticle and substrate. Since the chemical states of both bulk components observed in the Au 4*f* core-level spectra for bulk Au crystallite and DT-passivated Au nanoparticles are considered to be equivalent, the bulk components in the DT-passivated Au nanoparticles on the HOPG substrates correspond to the shifted ones of bulk component observed in the bulk Au crystallite due to the dynamic final-state effect. In order to analyze the present Au 4*f* core-level photoemission spectra of DT-passivated Au nanoparticles on the HOPG substrates, we apply the dynamic final-state model to Au 4*f* core-level photoemission spectra again. Figure 1 shows the comparison of experimental bulk component in the Au $4f_{7/2}$ core-level spectrum of DT-passivated Au nanoparticles with mean diameter of 3 nm on the HOPG substrates and calculated one from the experimental bulk component of bulk Au crystallite using dynamic final-state effect model. At the middle spectra in Fig. 1, the decomposed component denoted by red line shows the bulk component. The bottom spectrum shows the calculated bulk component based on the dynamic final-state effect on the bulk component of bulk Au crystallite. As shown in Fig. 1, the calculated bulk component reproduces the experimental one of DT-passivated Au nanoparticle on the HOPG substrate fairly well. Therefore, it is concluded that the experimental core-level photoemission spectral features of the present DT-passivated Au nanoparticles on the HOPG substrates can be also quantitatively characterized by the dynamic final-state effect model.

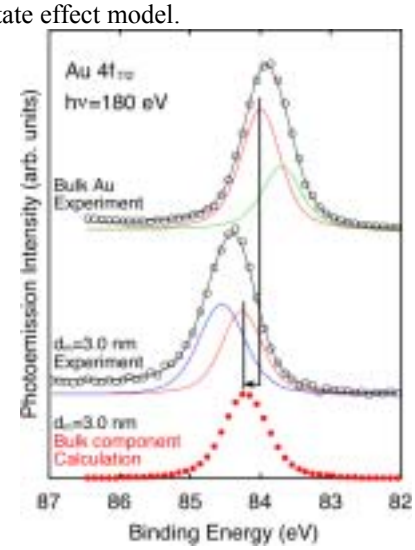

Fig. 1. Comparison of experimental Au $4f_{7/2}$ core-level spectrum of DT-passivated Au nanoparticles on the HOPG substrates and calculated one using dynamic final-state effect model.

[1] A. Tanaka, Y. Takeda, T. Nagasawa, and S. Sato, Phys. Rev. B **67**, 033101 (2003).
[2] A. Tanaka, Y. Takeda, T. Nagasawa, and K. Takahashi, Solid State Commun. **126**, 191 (2003).
[3] A. Tanaka, Y. Takeda, M. Imamura, and S. Sato, Phys. Rev. B **68**, 195415 (2003).

BL8B1, BL1A

Soft X-ray Absorption Spectra of Dilute Magnetic Semiconductor GaCrN

S. Emura[1], M. Hashimoto [1], H. Tanaka[1], M. S. Kim[1], S. Kimura[1],Z. Yikai [1], H. Asahi [1], Y. Arachi[2], H. Kobayashi[3]

[1]*ISIR, Osaka University, Mihoga-oka 8-1, Ibaraki, Osaka 567-0047,*

[2]*Faculty of Engineering, Kansai University, Suita Osaka 564-8680*

[3]*National Institute of Advanced Industrial Science and technology, Ikeda, Osaka 563-8577*

In present society, infrastructures of communication are demanded to expand in the speed and the quantity. One of future devices in this field is a spin-related device. Several candidates are considered and a part of those starts in fundamental research. Theoretical study also reveals the possibility of dilute magnetic semiconductor that exhibits ferromagnetism at room temperature and predicted that GaN-based dilute magnetic semiconductors, especially Cr-doped GaN, are highly potential candidates for those materials. This material, Cr doped wide gap semiconductor, shows ferromagnetic properties even at 400K experimentally. This is one of highest Curie temperatures at present in dilute magnetic semiconductors. Furthermore, GaCrN substance emits luminescence at the energy of near the band gap of Ga. We have, thus, three independent characters for GaCrN, semiconductor nature, ferromagnetism, and optical feature.

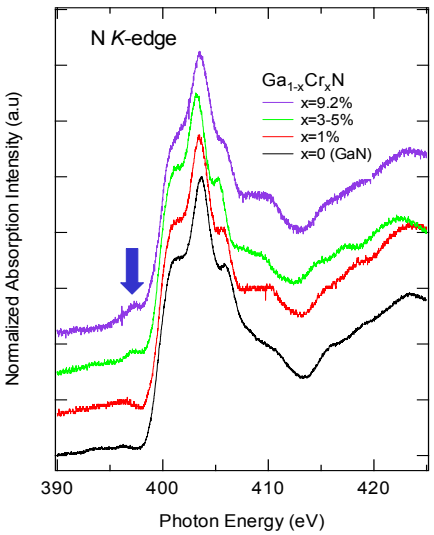

Fig.1 Absorption spectra around N *K*-edge of GaCrN.

Here, we observed the absorption spectra around N *K*-edge and Ga $L_{III,II}$-edge to try to reveal the origin of ferromagnetism of GaCrN. Figure 1 shows the absorption spectra around N *K*-edge. We found .a weak peak at 398eV lower than the fundamental N *K*-shell absorption edge for high Cr concentration specimens studied here. A blue arrow in Fig.1 indicates the peak. The intensity of the peak increases with the concentration of Cr atom. The 3*d*-orbitals of the doped Cr atom partially hybridize with the N 2*p*-orbitals to construct a valence band of GaCrN (Fig.2), and the other part makes a state in the band gap of GaCrN as the result of crystal field splitting. We tentatively assign the peak to a transition to the 3*d*-orbitals of Cr atom making the in-band gap state, which is essentially dipole-forbidden, but becomes partially dipole-allowed owing to the hybridization with the N *p*-orbital. The electrons in the in-band gap state may play the main role of ferromagnetism of GaCrN in connection of the hole of the valence band.

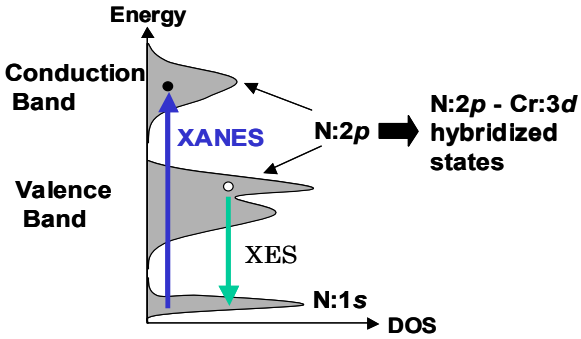

Fig.2 Schematic DOS of GaCrN and optical transition.

On the other hand, while a slight modification of the spectrum was found, indicated by a blue arrow, we did not observe the large change in the absorption spectrum around Ga L_{III}- and L_{II}-edges as shown in Fig.3. This observation means that the Ga and N s-orbital constructing the conduction band of GaCrN are not strongly affected by doping the Cr atom. By the way, the doped Cr atom states as trivalent ion in the GaN and constructs the alloy GaCrN. The configuration circumstance around the Cr ion has been elucidated with XAFS measurement, and the analysis indicates that the Cr ion locates substitutionally, but the first nearest neighbor configuration is somewhat complex.

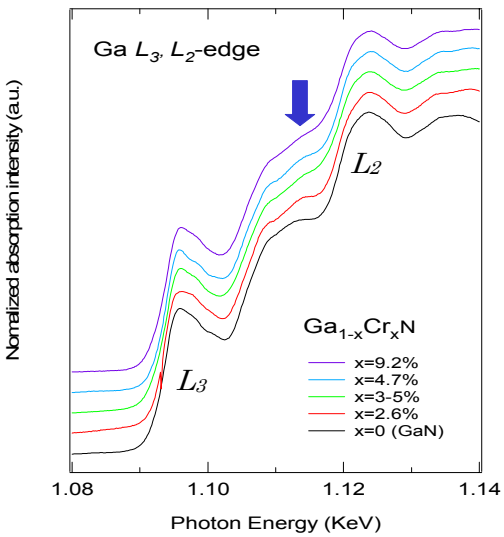

Fig.3 Absorption spectra around Ga L_{III} and L-$_{II}$-edge of GaCrN.

BL8B1

Study of Ar Cluster Ion Incident Angle for Super Hard Diamond Like Carbon Film Deposition

T. Kitagawa[1,2], K. Miyauchi[1], K. Kanda[2], Y. Shimizugawa[2], N. Toyoda[2], S. Matsui[2], H. Tsubakino[1], and I. Yamada[2,3]

[1] *Faculty of Engineering, Himeji Institute of Technology, Himeji, Hyogo, Japan*

[2] *Laboratory of Advanced Science and Technology for Industry, Himeji Institute of Technology, Kamigori, Hyogo, Japan*

[3] *Collaborative Research Center for Cluster Ion Beam Process Technology, Osaka Science and Technology Center, Osaka, Japan*

We have demonstrated that gas cluster ion beam (GCIB) assisted deposition was useful for forming super hard DLC films (> 50 GPa) with a smooth surface and low content of sp^2 orbital at room temperature [1,2].

In our case, the DLC films were formed with irradiation of Ar cluster ion beam during evaporating C_{60} as a carbon source. These films were deposited with a perpendicular irradiation of Ar cluster ions [3]. In this paper, effects of the irradiation angle of the Ar cluster ion beam on carbon film properties were studied, in order to develop this deposition technique and to optimize the angles for the super hard DLC film formation.

Result and Discussion

Figure 1 shows the NEXAFS spectra of the films irradiated with various incident angles of Ar cluster ion at the acceleration energy of 5 keV. Additionally, the spectra of the conventional DLC film formed with RF plasma and a diamond film formed with microwave plasma are also shown as references.

A significant difference of the spectra between DLC films and the diamond film was the pre-edge peak at 285.3 eV. This pre-edge resonance is due to transitions from a C_{1s} orbital to an unoccupied π^* orbital originating in *sp* and sp^2 orbitals. Thus, the NEXAFS spectrum of the diamond film, which has no- sp^2 orbital, did not present the pre-edge peak at all. This pre-edge peak is usually considered as a marker for presence of the sp^2 orbital, as the *sp* orbital is unstable. The increasing of the sp^2 content in the DLC film indicates the increasing the graphitic bond in the film. Therefore, in order to obtain higher hardness, the fraction of the sp^2 content in the DLC film should decrease. In the DLC films deposited with Ar cluster ion beam assistance, the peak shape at pre-edge of 285.3 eV was different between 0^o and 60^o. In comparison with the film at the normal incidence, the spectra of the film formed with incident angle of 60^o presented an increase of the peak width with the same peak intensity. Therefore, from Fig.1, the sp^2 content at60^o was higher than that at normal incident angle. At 40^o, the shoulder peak around 287 eV was also higher than that at normal. This increase is also concerned with increasing of sp^2 content, because the spectrum of the diamond does not have this shoulder peak. Thus, increasing of the incident angle increased the sp^2 content. Additionally, it should be noted that the sp^2 content of the film formed with normal incident angle was lower than that of RF plasma film.

Acknowledgements

The authors would like to appreciate Dr. Eiken Nakamura for operation of the beam line at UVSOR. This work is supported by New Energy and Industrial Technology Development Organization (NEDO) and the Joint Studies Program of the Institute for Molecular Science.

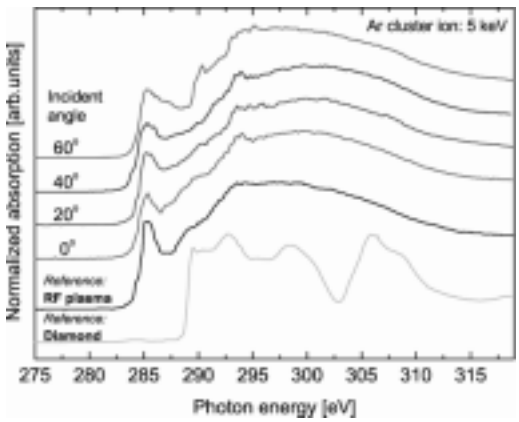

Figure 1: NEXAFS spectra of DLC films formed by Ar cluster ion beam assisted irradiation with oblique incident angles.

[1] Yamada, T. Kitagawa, J. Matsuo, and A. Kirkpatrick: Proceedings of the International Conference on the Mass Charge Transport in Inorganic Materials (2000) 957.

[2] T. Kitagawa, I. Yamada, N. Toyoda, H. Tsubakino, J. Matsuo, G.H. Takaoka, and A. Kirkpatrick: Nucl. Instrum. Methods Phys. Res. B **201** (2003) 405.

[3] T. Kitagawa, K. Miyauchi, K. Kanda, Y. Shimizugawa, N. Toyoda, H. Tsubakino, S. Matsui, J. Matsuo, and I. Yamada: Jpn. J. Appl. Phys. **42** (2003) 3971.

BL8B2

Angle-resolved UV Photoelectron Spectra of Thin Films of Perylene-3,4,9,10-tetracarboxylic Bisimidazole on GeS(001)

H. Yamane, M. Ohyama, H. Fukagawa, S. Kera*, D. Yoshimura**
K. K. Okudaira, A. Kahn***, K. Seki**, and N. Ueno
Faculty of Engineering, Chiba University, Chiba 263-8522 Japan
**Institute for Molecular Science, Okazaki 444-8585 Japan*
***Research Center for Materials Science, Nagoya University, Nagoya 464-8602 Japan*
****Department of Electrical Engineering, Princeton University, New Jersey 08544 USA*

Recently, we observed the intermolecular energy-band dispersion of the oriented perylene-3,4,9,10-tetracarboxylic dianhydride (PTCDA) multilayer[1]. The observed energy-band dispersion gave that the transfer integral for the π-π interaction (0.05 eV), the effective mass of HOMO hole (5.28 m0), and the hole mobility (> 3.8 cm2/V s, when τ > ħ/kBT), which are the fundamental basis for the understanding of electronic and optical properties of organic solids[1]. This was the first observation of the intermolecular energy-band dispersion of a conventional single-component organic semiconductor only with the weak intermolecular van der Waals interaction.

In this work, in order to obtain information on the intermolecular interaction of perylene-3,4,9,10-tetracarboxylic bisimidazole (PTCBI), we characterized the film structure of PTCBI thin films prepared on GeS(001) single crystal surface by measuring the take-off angle (θ) and the azimuthal (□) dependencies of angle-resolved UV photoelectron spectroscopy (ARUPS).

Experiments

ARUPS spectra were measured at photon incidence angle α = 0°, *hν* = 40 eV, and T = 295 K. θ and ϕ dependencies of ARUPS spectra were analyzed using the independent-atomic-center (IAC/MO) and the single-scattering (SS/MO) approximations combined with molecular orbital calculation[2].

A GeS(001) was cleaved in UHV. The cleanness of GeS(001) was confirmed by measuring ARUPS and low-energy electron diffraction (LEED). The purified PTCBI was carefully evaporated onto GeS(001). The film thickness and the deposition rate (< 1.0 Å/min.) were measured with a quartz microbalance.

Results and Discussion

Figure 1 (a) shows θ dependence of ARUPS of PTCBI (3Å) on GeS(001) substrate surface, where the intensity is normalized to the incidence photon flux, and the binding energy (E_B) is measured from the Fermi level of the substrate (E_F^{sub}). θ dependencies of ARUPS spectra are clearly seen. From MO calculation, the highest occupied molecular orbital (HOMO, E_B = 1.8 eV) band is assigned to a single π MO as shown in Fig. 1. This HOMO-band intensity showed maximum at θ = 30 ~ 33°.

Figure 1 (b) shows the comparison between observed and calculated θ dependencies of the HOMO-band intensities with the SS/MO (PM3) for the molecular tilt angle of β = 0°, which gave the best agreement with the observed θ pattern. It indicates that PTCBI molecules orient with their molecular plane parallel to the GeS(001) substrate surface. Furthermore, LEED measurements showed similar pattern from 3-Å- to 50-Å-PTCBI (not shown). Therefore, the strong intermolecular π-π interaction in PTCBI multilayer can be expected.

In order to obtain the energy-band dispersion in PTCBI multilayer, the measurements of θ, ϕ, and *hν* dependencies as a function of PTCBI deposition amounts are now in progress.

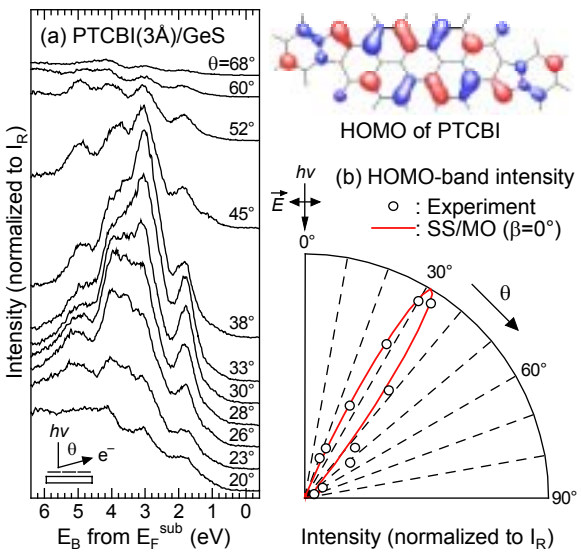

Fig. 1. (a) The take-off (θ) angle dependence of the ARUPS of the 3-Å-PTCBI on GeS(001). The intensity is normalized to the incidence photon flux. The binding energy (E_B) is measured from the Fermi level of the substrate (E_F^{sub}). (b) Comparison between observed and calculated θ dependencies of the HOMO-band intensities with the SS/MO (β = 0°).

[1] H. Yamane, S. Kera, K.K. Okudaira, D. Yoshimura, K. Seki, N. Ueno: Phys. Rev. B, 68 (2003) 033102.
[2] N. Ueno, A. Kitamura, K.K. Okudaira, T. Miyamae, Y. Harada, S. Hasegawa, H. Ishii, H. Inokuchi, T. Fujikawa, T. Miyazaki, K. Seki: J. Chem. Phys., 107 (1997) 2079.